Re-entry Target Identification with RCS Measurements Considering Multi-radar Geometry

Sung-Joo Lee
Mechanical & Control Eng.
Handong University
Pohang, Republic of Korea
sungjoo.lee@handong.ac.kr

Boyoung Jung
Mechanical & Control Eng.
Handong University
Pohang, Republic of Korea
boyoung@handong.ac.kr

Seung-Jin Park
Agency for Defense Development
Seoul, Republic of Korea
s.park@add.re.kr

Won-Sang Ra
Mechanical & Control Eng.
Handong University
Pohang, Republic of Korea
wonsang@handong.ac.kr

***Abstract*—This paper addresses the problem of re-entry target identification using radar cross section (RCS) measurements obtained from distributed radars. Considering that the RCS pattern is subordinate to the target class and the aspect angle, the target identification problem is formulated as maximum a posteriori estimation associated with the multiple hypothesis of these two unknowns. Once each hypothesis is propagated through the approximate aspect angle dynamics, the corresponding hypothesis probability is evaluated by using the available RCS measurements and the pre-trained RCS distribution for the corresponding hypothesis. To improve the target identification performance, the RCS measurement likelihood is calculated by exploiting the geometric relation between the target and the multi-radar. Computer simulations are carried out to demonstrate the superiority and reliability of the proposed method over the existing machine-learning based algorithm.**

***Index Terms*—Re-entry target identification, multi-radar, multiple hypothesis testing, radar cross section, hidden Markov model**

NOMENCLATURE

$\boldsymbol{p}_t^I, \boldsymbol{v}_t^I$	target position and velocity vectors
r	target range
v, v_g	target's total and ground speeds
γ_h, γ_v	target's flight path angles in horizontal/vertical plane
$L_{i,k}$	target aspect angle of the i^{th} radar
$\boldsymbol{L}_k$	aspect angle vector
α, β, α_T	angle of attack, sideslip angle, total angle of attack
t	track information provided by the multiple radars
$\tilde{\sigma}_{i,k}$	RCS measurement of i^{th} radar
$z_{i,k}$	RCS measurement sequence of i^{th} radar
$\boldsymbol{z}_k, \boldsymbol{Z}^k$	RCS measurement vector and its cummultation
$S_{i,k}$	section of the aspect angle for i^{th} radar
$\boldsymbol{S}_k$	vector of $S_{i,k}$ for multiple radars
C_k	target class
$\mathcal{N}(\boldsymbol{L}; \mu, \boldsymbol{\Sigma})$	normal distribution of $\boldsymbol{L}$, with mean μ and covariance $\boldsymbol{\Sigma}$

I. INTRODUCTION

Missile defense (MD) systems have played an important role in neutralising the ballistic missile threat. It is well known that efficient resource management of distributed radar systems is essential to enhance the anti-ballistic missile capability of a MD system [1]. This can be achieved by identifying the target of interest as early as possible. Since the target signature obtained from a radar depends on the shape of the target, most target identification algorithms have adopted the machine learning technologies using the available radar cross section (RCS) data. However, the existing algorithms may be restrictive in real applications because their performance is very sensitive to the authenticity of the test scenario or training data used for learning as well as to uncertainties in prior knowledge of the target's RCS pattern [2]–[5]. Therefore, a reliable radar target identification method is required to advance the MD system.

The existing radar target identification algorithms can be classified into two categories: single-frame and multi-frame methodologies [6]. Single-frame techniques, which are typically applied to high-resolution radars, employ the target signature at a specific time for target identification. One of the most common approaches to identify the target using high-resolution range profile (HRRP) [7]–[12]. These algorithms involve two primary steps: target feature extraction and target identification. In the first stage, low-dimensional intrinsic features of the target are extracted from the HRRP through various deep learning models such as the convolutional neural network, stacked corrective auto-encoders and so on. Then, in the second stage, the target identity (ID) is determined by assessing the similarity of the acquired features with the prior knowledge using the well-known machine learning algorithms (e.g. transfer learning, linear support vector machine, k-nearest neighbor). The prerequisite for this stage is that the feature distribution for the target class of interest has already been constructed. While this method provides satisfactory target identification performance in high signal-to-noise ratio (SNR) environments, its performance could be severely deteriorated in the presence of the translation or rotation errors in acquiring the HRRP information and the uncertainties of the constructed HRRP database [8].

Meanwhile, as an another single-frame technique, the target identification using micro-Doppler has also been attempted by many researchers [13], [14]. The underlying idea of this technique is that the precession, nutation, or spiral motion of the warhead of a re-entry target produces microscopic Doppler shifts. While this approach is effective in distinguishing the

This work was supported by the Agency for Defense Development by the Korean Government(UI247003TD).

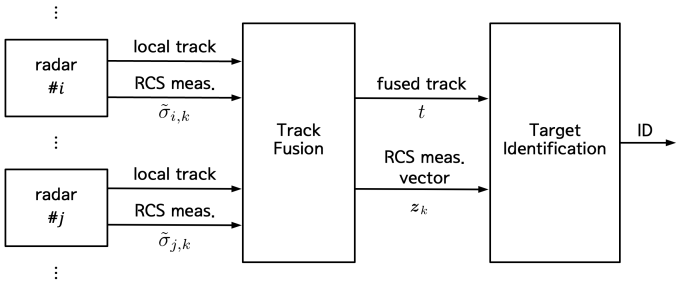

Fig. 1: Target identification schematic

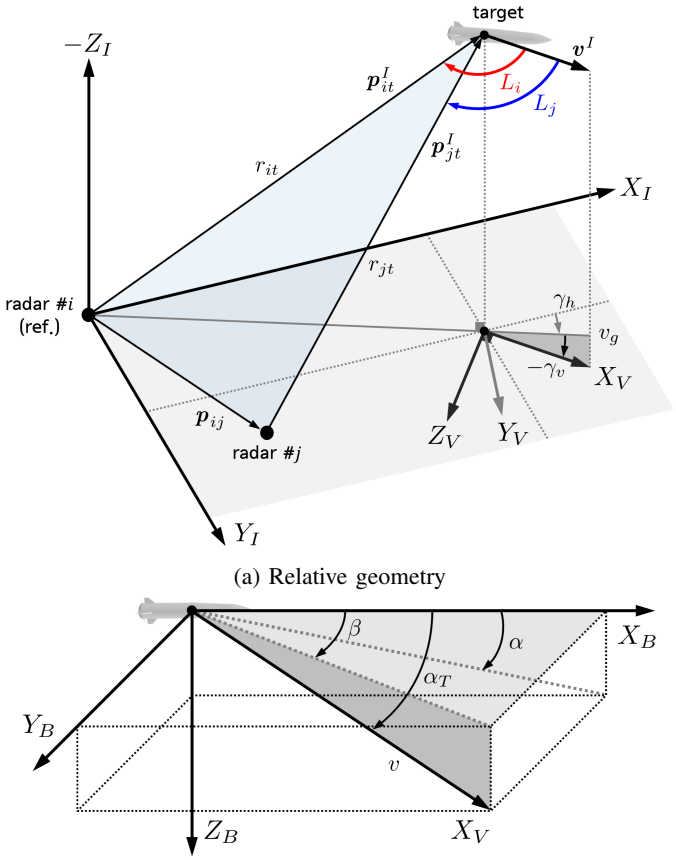

(a) Relative geometry

(b) Definition of angle of attack

Fig. 2: Coordinate systems

warhead from the debris or decoys, it is not suitable for identifying the class of a ballistic missile whose motion varies with the guidance and control strategies.

As an alternative to the single-frame algorithms, the multi-frame target identification algorithms that utilize the signature information acquired continuously over a certain period of time have been proposed. Since these approaches obtain additional features of the target from the time series of the signature information, applications can be achieved not only with a high-resolution radar, but also with a low-resolution radar which only provides RCS. Unfortunately, in this case, target identification could become more complex because the aspect angle changes during the acquisition of the RCS measurement sequence. To solve the problem, the hidden Markov model (HMM) methods was applied [2], [3], [15]–[17]. This approach considered the section of aspect angles from which the RCS measurements were obtained as an unknown hidden state. While this method provides the possibility of target identification even when the aspect angle changes, it inevitably introduces the issue of sensitivity to the training trajectory. In other words, if the actual target trajectory is different from the trajectory used for training, it is difficult to ensure satisfactory target identification performance with HMM-based algorithms.

As a remedy for these technical challenges, a multi-hypothesis re-entry target identification algorithm that utilises the RCS data from multiple radars is proposed in this paper. To ensure the robustness of the algorithm in the presence of the uncertainties in the distribution of the RCS pattern and variations in the aspect angle, we incorporate the target state estimate from the tracking filter as auxiliary information. This is because the target's angle of attack remains relatively small during the re-entry phase, allowing the target state estimate to outline the predicted aspect angle and its dynamics. To account for the influence of the target's angle of attack, the aspect angle hypotheses are generated to estimate the actual aspect angle relative to the predicted aspect angle, and a transition model of the aspect angle is derived using the aspect angle dynamics. Consequently, the problem of identifying the re-entry target is reduced to the maximum *a posteriori* probability (MAP) estimation for a composite hypothesis of the target class and the aspect angle, based on a sequence of RCS measurements. This is done by using a model of the distribution of RCS measurements per section of the aspect angle and by considering the transition of the aspect angle. Since the target identification performance may be adversely affected by ambiguity in the RCS pattern between target classes in certain regions of aspect angle, we actively use the fusion tracks of multiple radars as prior information to mitigate this problem. To this end, the likelihoods of the measurements from the distributed radars are then fused based on the geometric constraints on the probable target aspect angles of multi-radar and update the posterior probability. In addition, to reduce the computational workload of generating hypotheses and to enable real-time implementation of the proposed algorithm, hypotheses with identical aspect angle transition histories are combined. This idea is based on the fact that the sequence of RCS measurements acquired will inevitably be contingent upon the history of aspect angle. Through computer simulations for typical re-entry target tracking scenarios, we compare and analyse the re-entry target identification performance between the proposed method and the existing HMM method.

II. Target Identification Problem Statement

The RCS data is an important target signature that is calculated through radar signal processing. It is important to note that RCS measurements acquired from radar are highly influenced by physical elements such as target shape and

material, which can be used to identify the re-entry target. The RCS pattern differs not only between re-entry target classes but also based on the incident angle of the radar or the target posture. Therefore, the re-entry target identification problem must be defined in terms of changes in the radar aspect angle.

A. Definition of Target Aspect Angle

For simplicity, consider the relative geometry between the target and the multiple radars, as depicted in Fig. 2a. The notations used in the figures are defined as follows:

$$\boldsymbol{p}_t^I = \begin{bmatrix} x & y & z \end{bmatrix}^T, \quad \boldsymbol{v}_t^I = \begin{bmatrix} v_x & v_y & v_z \end{bmatrix}^T, \quad r = |\boldsymbol{p}_t^I| \quad (1)$$

where (x, y, z) and (v_x, v_y, v_z) is the relative position and velocity of the target with respect to the radar.

In addition, the definitions of the coordinate systems used to describe the relative geometry are given in Table I. All frames used in this paper follow the conventional right-hand rule. In the table, $R_\chi(\varepsilon)$ represents the rotation matrix with respect to χ-axis by an angle ε, and C_a^b is the coordinate transformation matrix from the a-frame to the b-frame.

In order to model the RCS characteristics, it is necessary to define the aspect angle of the target. The aspect angle, illustrated on the Fig. 2a, can be derived by the inner product of the target nose direction and the target position vector.

$$\boldsymbol{u}_X^B = C_V^B C_I^V \boldsymbol{u}_X^I, \quad L = \cos^{-1}\left(-(\boldsymbol{p}_t^I \cdot C_B^I \boldsymbol{u}_X^B)/r\right) \quad (2)$$

where $\boldsymbol{u}_X^B$ and $\boldsymbol{u}_X^I$ is the unit vector direction to X_B and X_I.

However, in the re-entry phase of the target, the total angle of attack α_T is kept to a relatively small value, which results that the target's posture can be approximated to the direction of the velocity vector. From the (2), the aspect angle of the target can be redefined as follows.

$$\boldsymbol{u}_X^B \approx C_I^V \boldsymbol{u}_X^I, \quad L \approx \cos^{-1}\left(-(\boldsymbol{p}_t^I \cdot \boldsymbol{v}_t^I)/(rv)\right) \quad (3)$$

TABLE I: Definitions of coordinate systems

Frame	Definition
I	Inertial frame with the origin located on the reference radar X_I: True north direction Y_I: True east direction Z_I: Vertical downward of the Earth's plane
V	Target velocity frame with the origin at the target's centre of gravity X_V: Velocity vector direction Y_V: on the horizontal plane in the I-frame $C_I^V = R_y(\gamma_v)R_z(\gamma_h)$ $\gamma_h = \tan^{-1}(v_y/v_x)$, $\gamma_v = \tan^{-1}(-v_z/v_g)$, $v_g = \sqrt{v_x^2 + v_y^2}$
B	Target body frame with the origin at the target's centre of gravity X_B: Target nose direction $C_I^B = R_x(\phi)R_y(\theta)R_z(\psi)$ ϕ, θ, ψ: target roll, pitch, yaw

B. RCS Sequence based Target Identification

Identifying a target from a single frame of RCS measurement is challenging due to the significant variation in target RCS with aspect angle, uncertainty in target posture, and the inherent measurement noise.

To mitigate the sensitivity to the aspect angle variability and measurement noise, we propose the target identification method using the statistical distribution of the RCS measurement sequence. The RCS signature can be modelled into a function with the aspect angle using the RF analysis tool given by the 3D CAD model of the target, considering its geometric and material properties. The RCS measurements are generated by incorporating the Chi-squared distribution based measurement noise. The variational Gaussian mixture model is used to train the nonlinear distribution of RCS measurements.

The distribution of RCS measurements within each angular section exhibits class-specific characteristics and is relatively insensitive to measurement noise, target posture and target specification uncertainty. Thus, the likelihood between the pre-trained distribution and the RCS measurement sequence serves as crucial information for target identification. However, for angular sections near 90°, the RCS measurement distributions between classes become similar due to small variations in target geometric, posing a challenge for target identification. To address this, measurements from multiple target allocated in different locations can be fused to overcome such limitations. In addition, geometric constraints derived from fused track information and radar locations improve the robustness of identification against target posture uncertainty.

If the aspect angle is known, the likelihood of the acquired RCS measurement sequence can be calculated using the distribution of identified targets for that angle section. Unfortunately, the aspect angles that characterise the distribution of RCS measurements cannot be known in practice because they are a function of the relative position of the radar to the target and the attitude of the target. Furthermore, the aspect angle is constantly changing during the translational and angular motion of the re-entry target, making it difficult to accurately identify the target using the above concepts.

In this regard, re-entry target identification using RCS is reduced to the problem of inferring the time-varying angular sections along with the target classes. That is, for a given set of target classes $\mathcal{H}_C$ and a set of angular sections $\mathcal{H}_S$, we define a hypothesis as $(C \in \mathcal{H}_C, S \in \mathcal{H}_S)$, and then branch the hypotheses over time to determine which is the most likely. As there is no transition between target classes, the change in the sequence of RCS measurements is determined by the angular section transition. Therefore, target identification is performed by comparing the probabilities between class hypotheses with the same angular transition history. Note that the number of hypotheses increases drastically due to the angular section hypothesis transition. For such case, it is impossible to find the optimal solution to the target identification problem due to computational restriction. Therefore, to implement a target identification algorithm, a hypothesis management technique is required to suppress the growth of the number of hypotheses.

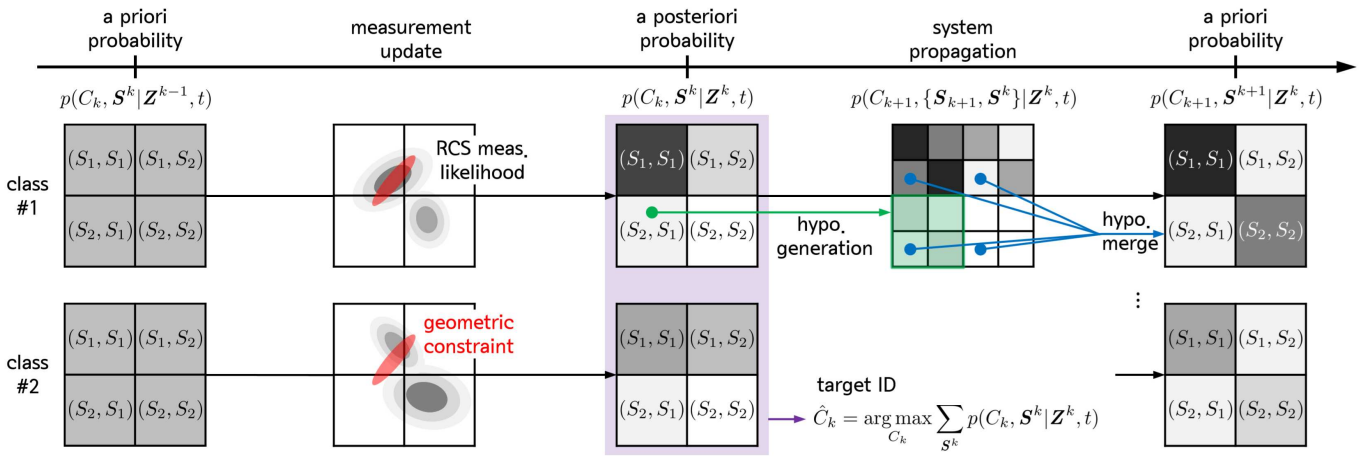

Fig. 3: Target identification based on multi-radar RCS measurements and geometric constraints

Problem 1 ***(Target Identification using Multi-radar)*****:** Given the RCS measurement sequence and the geometric constraints, find the target class which maximises

$$\hat{C}_k = \arg\max_{C_k} p(C_k|\boldsymbol{Z}^k, t) \tag{4}$$

where C is the target class, $\boldsymbol{Z}$ is the cumulative RCS measurement sequence vector, and t is the fused track information.

III. Target Identification Algorithm

This section presents the design of the target identification algorithm described above. Corresponding to the change in aspect angle, the multiple-hypothesis based aspect angle transition and hypothesis evaluation methodology is used.

A. Probability Space Construction for Target Identification

- Hypothesis Generation

Let us define the target class C_{k-1} and the sequence of angular section hypothesis S^{k-1} at time instant $k-1$. As we have assumed no transitions between the target classes, the hypothesis furcates from (C_{k-1}, S^{k-1}) to $(C_k, S^k \triangleq \{S^{k-1}, S_k\})$ according to the transition of aspect angle section. In the case of a re-entry target, since the total angle of attack is typically limited to within $10°$, which is a predetermined aspect angular section for the entire flight, we can approximate the aspect angle $\hat{L}_k$ at time instant k in (3) using the state variable estimates provided by the tracking filter. If the aspect angle satisfies $\hat{L}_k \in (S_k = h)$, then the set of hypotheses at time instant k comprises the l adjacent sections $\{h-l, \ldots, h-1, h, h+1, \ldots, h+l\}$ centred on $S_k = h$.

- Hypothesis Evaluation

To identify the target, we statistically evaluate the RCS measurements $\tilde{\sigma}$ from each radar against the generated hypothesis (C_k, S^k). The accuracy of target identification may be degraded by the use of a single measurement frame due to the various uncertainties in the RCS measurement. Therefore, we set the identification algorithm period T longer than that of the radar and used n RCS measurements $z_k \equiv \{\tilde{\sigma}_1, \ldots, \tilde{\sigma}_n\}$ collected during the identification period.

When the RCS measurements z_k is equipped, the *a posteriori* probability against the hypothesis (C_k, S^k) can be computed using Bayes' theorem:

$$p(C_k, S^k|Z^k) = \frac{p(z_k|C_k, S_k)p(C_k, S^k|Z^{k-1})}{p(z_k|Z^{k-1})} \tag{5}$$

If the noise in RCS measurements is independent at each moment and the following equation is satisfied.

$$p(z_k|C_k, S_k) = \prod_{t=1}^{n} p(\tilde{\sigma}_t|C_k, S_k) \tag{6}$$

If the transition of the angular section is assumed as a first-order Markov model, from (5), the *a priori* probability $p(C_k, S^k|Z^{k-1})$ is rewritten as follows.

$$p(C_k, S^k|Z^{k-1}) = p(S_k|S_{k-1})p(C_{k-1}, S^{k-1}|Z^{k-1}) \tag{7}$$

where $p(S_k|S_{k-1})$ denotes the transition probability from angular section hypothesis S_{k-1} to S_k, and $p(C_{k-1}, S^{k-1}|Z^{k-1})$ is obtained recursively by (5).

To calculate the transition probability $p(S_{k+1}|S_k)$, we induce the dynamics of the aspect angle. With the state variable $\boldsymbol{x}$, which contains the position and velocity of the re-entry target, the aspect angle L can be expressed as a function $L = g(\boldsymbol{x})$ as (3). The dynamics of the state variable $\boldsymbol{x}$ can be described by the following nonlinear differential equation according to the motion of the re-entry target.

$$\dot{\boldsymbol{x}} = f(\boldsymbol{x}) + \boldsymbol{w}, \quad \boldsymbol{w} \sim N(0, Q) \tag{8}$$

For example, for the target in ballistic motion, the state variable $\boldsymbol{x}$ and the nonlinear differential equation $f(\cdot)$ are defined as follows [18], [19].

$$\boldsymbol{x} \triangleq \begin{bmatrix} x \\ y \\ z \\ v_x \\ v_y \\ v_z \\ \alpha_D \end{bmatrix}, \quad f(\boldsymbol{x}) \triangleq \begin{bmatrix} v_x \\ v_y \\ v_z \\ -\frac{1}{2}\rho(h)v\alpha_D \begin{bmatrix} v_x \\ v_y \\ v_z \end{bmatrix} + \begin{bmatrix} 0 \\ 0 \\ g \end{bmatrix} \\ 0 \end{bmatrix}$$

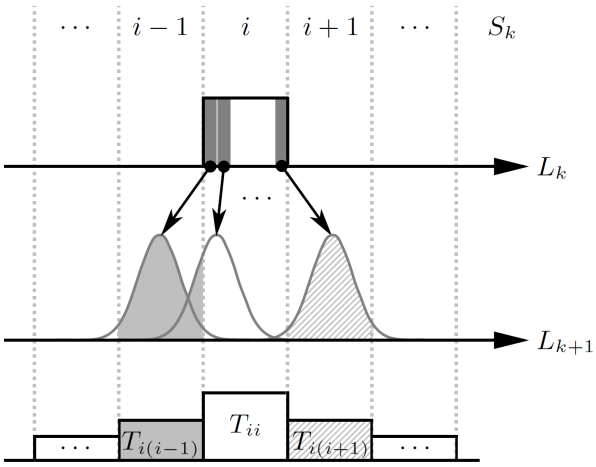

Fig. 4: Aspect angle transition probability calculation

where ρ is the air density at height h, α_D is the drag coefficient which the reference area and mass of the target is considered, and g is the gravitational acceleration constant.

Thus, by differentiating (3) and substituting (8), the dynamics of the aspect angle can be described as follows:

$$\dot{L} = \frac{\partial g(\boldsymbol{x})}{\partial \boldsymbol{x}}\dot{\boldsymbol{x}} = \frac{\partial g(\boldsymbol{x})}{\partial \boldsymbol{x}}[f(\boldsymbol{x}) + \boldsymbol{w}], \tag{9}$$

where the process noise $\boldsymbol{w}$ in (9) is an additive white Gaussian noise (AWGN), the stochastic characteristic of $\dot{L}$ follows.

$$\dot{L} \sim N\left(\frac{\partial g(\boldsymbol{x})}{\partial \boldsymbol{x}} f(\boldsymbol{x}), \left(\frac{\partial g(\boldsymbol{x})}{\partial \boldsymbol{x}}\right) Q \left(\frac{\partial g(\boldsymbol{x})}{\partial \boldsymbol{x}}\right)^T\right) \tag{10}$$

Discretising (9) with the identification period T, we can derive the predicted aspect angle at time instant $k+1$.

$$L_{k+1} \approx L_k + T\dot{L}_k = g(\boldsymbol{x}_k) + T\frac{\partial g(\boldsymbol{x}_k)}{\partial \boldsymbol{x}_k}[f(\boldsymbol{x}_k) + \boldsymbol{w}_k] \tag{11}$$

The process of calculating $p(S_{k+1} = j | S_k = i)$ is illustrated in Fig. 4. The ith aspect angular section $(S_k = i)$ at time instant k is dived into M equal parts, and the probability of the mth part of the aspect angular section $L_{m,k}$ is denoted as follows.

$$p(L_k = L_{m,k} | S_k = i) = \frac{1}{M}, \quad m = 1, \ldots, M \tag{12}$$

If $L_k = L_{m,k}$, we can approximate the distribution of each part $p(L_{k+1} | L_k = L_{m,k})$ with respect to L_{k+1} using (11). The first and second moments follow.

$$\begin{aligned} E(L_{k+1} | L_k = L_{m,k}) &= L_{m,k} + T \cdot E(\dot{L}_k), \\ var(L_{k+1} | L_k = L_{m,k}) &= T^2 \cdot var(\dot{L}_k) \end{aligned} \tag{13}$$

The transition probability $T_{ij} = p(S_{k+1} = j | S_k = i)$, which denotes the transition from the ith to the jth angular section from time instant k to $k+1$, can be calculated by integrating the distribution $p(L_{k+1} | L_k = L_{m,k})$ with respect to the divided angular sections.

$$T_{ij} = \int \sum_{m=1}^{M} p(L_{k+1} | L_k = L_{m,k}) dL_{k+1} \tag{14}$$

where the integration is performed within the aspect angle section $(S_{k+1} = j)$.

- Hypothesis Merging

To prevent an exponential increase in the number of generated hypotheses over time, we use the 1-SB (scan-back) hypothesis management technique. Firstly, we calculate the *a posteriori* probability of the hypothesis $S^k = \{S_{k-1}, S_k\}$, which represents the transition from the aspect angle section S_{k-1} to S_k at time instant $k-1$ to k. Then, the hypotheses are merged with the same aspect angle section at time instant k as $S^k = S_k$ before generating hypothesis onto $k+1$.

B. Performance Improvement using Geometric Constraint

The geometric constraints between the radars can be utilised for the hypothesis evaluation. To take into account the constraints imposed by multiple radars, the probability space is reconstructed under the following assumptions:

A1. Track information is fused in the track fusion stage, under the synchronized radar.

A2. Fused track information and the RCS measurements are processed in different sectors, independently.

The radars satisfy the following geometric constraint.

$$r_{it} \cos L_i - r_{jt} \cos L_j = -\boldsymbol{p}_{ij} \cdot \boldsymbol{u}_v^I \tag{15}$$

where r_{it} is the relative distance from the i^{th} radar to the target, L_i is the aspect angle of target observed by the i^{th} radar, $\boldsymbol{p}_{ij}$ is the vector from the position of the i^{th} radar to the j^{th} radar, and the $\boldsymbol{u}_v^I$ is the unit vector for velocity of target in I-frame.

Given the RCS measurement vector $\boldsymbol{z}_k \triangleq [z_{i,k}\ z_{j,k}]^T$, the *a posteriori* probability, in (4), can be expanded against to the hypothesis vector $(C_k, \boldsymbol{S}^k \triangleq [S_i^k\ S_j^k]^T)$:

$$p(C_k, \boldsymbol{S}^k | \boldsymbol{Z}^k, t) = \frac{1}{c} p(\boldsymbol{z}_k | C_k, \boldsymbol{S}_k) p(\boldsymbol{S}_k | t) p(C_k, \boldsymbol{S}^k | \boldsymbol{Z}^{k-1}, t) \tag{16}$$

where $\boldsymbol{Z}^k = \{\boldsymbol{z}_1, \ldots, \boldsymbol{z}_k\}$ is the cumulative RCS measurement vector from the radars, $p(\boldsymbol{z}_k | C_k, \boldsymbol{S}_k)$ is the likelihood of the RCS measurement vector, $p(\boldsymbol{S}_k | t)$ is the geometric constraints derived from the fused track information t, and c is the normalising constant. The *a posteriori* probability (16) can be calculated by the following steps.

Step 1. The likelihood of the RCS measurement vector can be calculated by considering their independence.

$$p(\boldsymbol{z}_k | C_k, \boldsymbol{S}_k) = p(z_{i,k} | C_k, S_{i,k}) p(z_{j,k} | C_k, S_{j,k}) \tag{17}$$

Step 2. The geometric constraint, depicted in Fig. 2, is considered by the uncertainty of the target posture and the fused track information. Based on the uniform distribution of the uncertainty in the angle of attack and sideslip, the constraint can be approximated into the sum of multivariate Gaussian distributions:

$$p(\boldsymbol{L}_k | t) = \sum_{n=1}^{N} w_n \mathcal{N}(\boldsymbol{L}; \mu_n, \boldsymbol{\Sigma}_n), \quad \sum_{n=1}^{N} w_n = 1 \tag{18}$$

By integrating the (18) over the joint angular section hypothesis with respect to the aspect angle, the geometric constraints of the fused track can be calculated asymptotically.

$$p(\boldsymbol{S}_k|t) = \int_{\boldsymbol{L}_k \subset \boldsymbol{S}_k} p(\boldsymbol{L}_k|t) d\boldsymbol{L}_k \tag{19}$$

Step 3. The normalising constant c of (16) can be formulated by the total probability theorem.

$$\begin{aligned} c &= p(\boldsymbol{z}_k|\boldsymbol{Z}^{k-1}, t) \\ &= \sum_{C_k, \boldsymbol{S}_k} p(\boldsymbol{z}_k|C_k, \boldsymbol{S}_k) p(\boldsymbol{S}_k|t) p(C_k, \boldsymbol{S}^k|\boldsymbol{Z}^{k-1}, t) \end{aligned} \tag{20}$$

As stated at the problem 1, the target ID is determined by the class hypothesis which maximises the *a posteriori* probability (16) marginalised by the angular section hypothesis.

$$\hat{C}_k = \arg\max_{C_k} \sum_{\boldsymbol{S}^k} p(C_k, \boldsymbol{S}^k|\boldsymbol{Z}^k, t) \tag{21}$$

IV. Simulation and Analysis

Simulations are conducted to validate the effectiveness of the proposed method, which utilises multiple radars with angular dynamics, on targets in the re-entry phase classified as C_1, C_2, and C_3. The RCS profiles of target classes with regard to the aspect angle are depicted in Fig. 5.

The analysis is focused on the target C_2, which has a medium-sized shape among the three classes. The RCS measurements from each radar i, j are obtained, and the parameters used for the simulation are listed in Table II. The state variable of the tracking filter comprises the three-dimensional position, velocity, and the drag coefficient of the target. The estimation of the drag coefficient is performed at every instant by the tracking filter. Furthermore, due to the challenge of accurately determining the target geometry and the level of measurement noise in real-world scenarios, there may be a discrepancy between the simulated and actual distributions of RCS measurements. To address this uncertainty, a bias error with a uniform distribution ranging from $3[dBsm]$ is added to the RCS measurements.

In order to demonstrate the efficacy of the proposed algorithm, we employ the HMM method for comparison, one of the representative ways of identifying the target [9]. The HMM-based target identification method trains the pattern of angular section transitions through the RCS measurement sequences. The trained model is used to identify the target by maximising the cumulative likelihood of RCS measurements. Two HMM models are trained using different datasets with varying aspect angle changes. The training dataset comprises 500 RCS sequences, each constructed from 10 target trajectories with 50 RCS measurement sequences. The results, designated HMM1 and HMM2, were trained using the aforementioned dataset, which exhibited a considerable degree of variation in aspect angle *(solid and dashed lines in Fig. 6a)*. The results of the training are presented in the form of a confusion matrix in Fig. 7, where the light grey rows represent the actual target classes and the dark grey columns represent the identified target class.

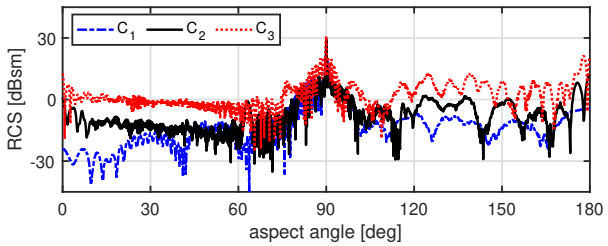

Fig. 5: RCS profiles of the target classes

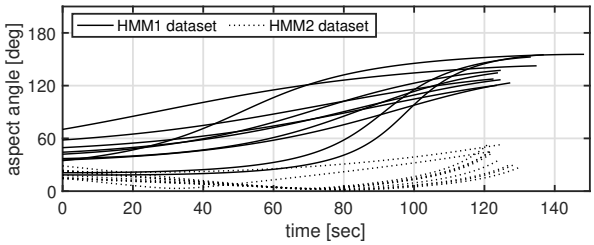

(a) training

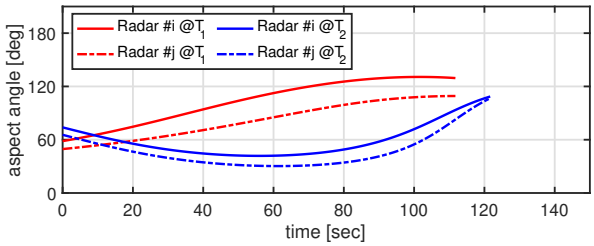

(b) validation

Fig. 6: Trajectory dataset used for training and validation

One of the inherent limitations of HMM-based target identification algorithms is their reliance on the trajectory scenarios employed for training. To account for the various factors that influence the variation of the aspect angle (including launch and impact points, radar position, etc.), a substantial number of target trajectories must be included in the training process. Consequently, the dependence on training trajectory scenarios is a crucial factor in evaluating the identification algorithm. Simulations were conducted for the test scenarios, as depicted in Fig. 6b, to demonstrate that the proposed method provides more reliable identification performance than the existing methods. The simulation results are based on 200 Monte-Carlo trials.

Fig. 8 depicts the identification rate against the target classes

TABLE II: Simulation condition

sampling period	$T_s = 0.05[sec]$
identification period	$T = 0.5[sec]$
std. of meas. noises (range/angle)	$\sigma_r = 200[m]$, $\sigma_\psi = \sigma_\theta = 0.2[deg]$
interval of the angular section	$10[deg]$
number of hypothesis	5

	C_1	C_2	C_3
C_1	0.86	0.14	0.00
C_2	0.18	0.82	0.00
C_3	0.00	0.19	0.81

(a) HMM1

	C_1	C_2	C_3
C_1	1.00	0.00	0.00
C_2	0.26	0.74	0.00
C_3	0.00	0.00	1.00

(b) HMM2

Fig. 7: HMM training result confusion matrix

T_1	C_1	C_2	C_3
C_1	0.75	0.25	0.00
C_2	0.13	0.87	0.00
C_3	0.00	0.22	0.78

T_2	C_1	C_2	C_3
C_1	0.99	0.01	0.00
C_2	0.77	0.23	0.00
C_3	0.01	0.47	0.52

(a) HMM1

T_1	C_1	C_2	C_3
C_1	0.07	0.93	0.00
C_2	0.42	0.58	0.00
C_3	0.00	0.15	0.85

T_2	C_1	C_2	C_3
C_1	0.95	0.05	0.00
C_2	0.49	0.51	0.00
C_3	0.01	0.33	0.66

(b) HMM2

T_1	C_1	C_2	C_3
C_1	0.94	0.06	0.00
C_2	0.07	0.93	0.00
C_3	0.00	0.00	1.00

T_2	C_1	C_2	C_3
C_1	0.93	0.07	0.00
C_2	0.03	0.97	0.00
C_3	0.00	0.01	0.99

(c) MAP

Fig. 8: Target identification results confusion matrix

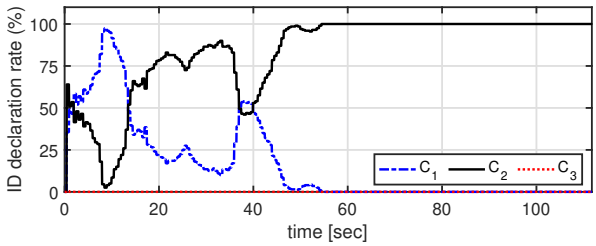

(a) radar i

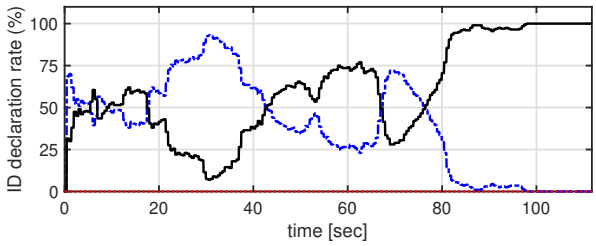

(b) radar j

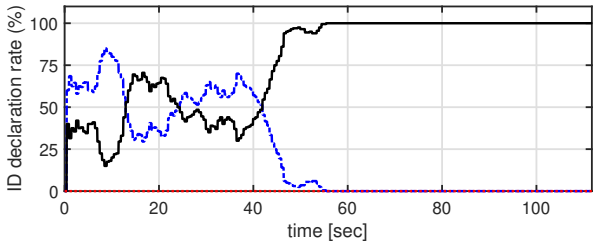

(c) likelihood fused

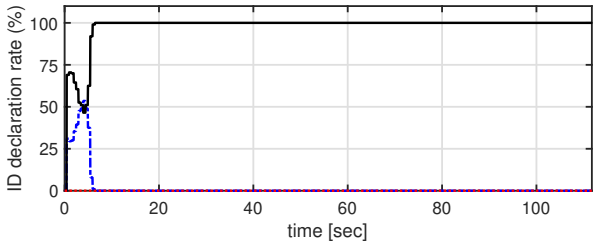

(d) proposed

Fig. 9: Target identification results of T_1 scenario

for each scenario. From Fig. 8a and 8b, the identification rate varies considerably for the test trajectory, which exhibits a different aspect angle variation in comparison to the training dataset. The HMM1 model is capable of identifying targets with at least 75% accuracy in the T_1 trajectory. Even the HMM2 model, which exhibits a lower performance in comparison to the HMM1 model, is capable of identifying targets with at least 51% accuracy in the T_2 trajectory. However, the HMM1 model identifies the C_2 target with 23% accuracy for the T_2 scenario, and the HMM2 model identifies the C_1 target with 7% accuracy for the T_1 scenario. This result demonstrates that the HMM-based identification method is contingent upon the training dataset. Nevertheless, as illustrated in Fig. 8c, the proposed identification algorithm demonstrates robust performance regardless of the test trajectory.

TABLE III: Required time for ID confirmation

	radar i	radar j	radar i, j	proposed
T_1	50.0$[sec]$	81.5$[sec]$	46.5$[sec]$	5.5$[sec]$
T_2	fail	57.0$[sec]$	59.5$[sec]$	4.0$[sec]$

In order to validate the superiority of considering the geometric constraints of multi-radar, the additional trajectory from the radar j is considered. Fig. 9 depicts the ID declaration rate of single and multi-radar in relation to the T_1 scenario. Fig. 9a and 9b illustrate the results of individual radars, whereas Fig. 9c depicts the performance when the RCS measurement likelihood is fused. Fig. 9d illustrates the result when the geometric constraint is also considered. The target ID is defined when the ID declaration rate meets the 90% accuracy threshold. To

facilitate a comparative analysis of the performance between the single and multi-radar configurations, the required time for ID confirmation is presented in Table III.

As illustrated in Fig. 5, the C_1 and C_2 targets are challenging to identify within the range of 50° to 100° of aspect angle due to the similar distribution of their RCS profiles. This is demonstrated in Fig. 9a and 9b as a performance of ID declaration rate. Referring to the trajectory of target T_1 as depicted in Fig. 6b, the aspect angle of the target observed from radar i lies within the ambiguous area. This results in an uncertain identification result until 46 seconds, which is also visible on the radar j, where an uncertain result is observed until 81 seconds. If only the RCS measurement likelihoods are considered, as depicted in Fig. 9c, the performance is enhanced from 46 to 81 seconds due to the distinctive RCS measurements from the radar i. However, until 41 seconds, as both radars observe the aspect angle of the target in an ambiguous area, the identification performance remains unsatisfactory. When the geometric constraint between the multi-radar and the target is considered, the identification performance is found to be significantly enhanced, even in the ambiguous time period between 5 and 41 seconds, as illustrated in Fig. 9d. From Table III, the T_2 scenario represents the most unfavourable outcome for radar i, where the identification fails. This results the poor performance, even when the measurement likelihoods are fused. However, when the geometric constraint is considered, the ID confirmation time is 4.0 seconds, which is a more favourable result than the other approaches.

V. CONCLUSION

A novel approach to re-entry target identification is proposed, which utilises RCS measurements obtained from multiple radars. The target identification problem is defined as the process of determining both the target class and the aspect angle of a sequence of RCS measurements provided by the radars within the framework of multiple hypothesis testing. The hypotheses on the target class and the aspect angle are propagated using the angular transition probabilities computed from the available target track, and merged with the same angular transition history for the real-time implementation of the proposed algorithm. To enhance the reliability of the target identification, the geometric constraints between the target and the multi-radar were used to update the hypothesis probability. Through simulations, it was shown that our method enhances the classification rate by an average of 31.3%, compared to the conventional HMM technique. Different from the conventional machine learning based algorithms, the proposed method is expected to be a practical solution to the radar target identification problem because it provides the satisfactory performance even when the actual target scenario differs from the trajectories used for training.

REFERENCES

[1] A. Carter, and D. Schwartz, Ballistic missile defense. Brooking Institution Press, 2010.

[2] K.-W. Yoo, J.-H. Chun, and B.-G. Choi, Target classification and tracking based on aerodynamic properties and RCS information using Rao-Blackwellized particle filter, in Conf. IEEE Photonics & Electromagnetics Research Symposium (PIERS), Xiamen, 2020, pp.146-154.

[3] B. Rao, Y.-L. Zhao, S.-P. Xiao, and X.-S. Wang, Discrimination of exo-atmospheric active decoys using acceleration information, IET radar, sonar & navigation, vol. 4, no. 4, Aug. 2010, pp.626-638.

[4] T. Wang, W. Bi, Y. Zhao, and W. Xue, Radar target recognition algorithm based on RCS observation sequence–Set-valued identification method, Journal of Systems Science and Complexity, vol. 29, Dec. 2015, pp.573-588.

[5] Y. Yang, Z. Zhang, W. Mao, Y. Li, and C. Lv, Radar target recognition based on few-shot learning, Multimedia Systems, Special no. Paper, Jul. 2021, pp.2865-2975.

[6] P. Tait, Introduction to radar target recognition. IET vol. 18, 2005.

[7] P. Wang, F. Dai, M. Pan, L. Du, and H. Liu, Radar HRRP target recognition in frequency domain based on autoregressive model, in Conf. IEEE RadarCon (RADAR), Missouri, 2011, pp.714-717.

[8] Y. Wen, L. Shi, X. Yu, Y. Huang, and X. Ding, HRRP target recognition with deep transfer learning, IEEE Access, vol. 8, Mar. 2020, pp.57859-57867.

[9] M. Dewitt, High range resolution radar target identification using the prony model and hidden markov models, Master dissertation, Air Force Inst. of Tech., Ohio, 1992.

[10] B. Feng, B. Chen, and H. Liu, Radar HRRP target recognition with deep networks, Pattern Recognition, vol. 61, Jan. 2017, pp.379-393.

[11] A. Persico, C. Ilioudis, C. Clemente, and J. Soraghan, Novel classification algorithm for ballistic target based on HRRP frame, IEEE Transactions on Aerospace and Electronic Systems, vol. 55, no. 6, Dec. 2019, pp.3168-3189.

[12] M. Pan, L. Du, P. Wang, H. Liu, and Z. Bao, Multi-task hidden Markov modeling of spectrogram feature from radar high-resolution range profiles, EURASIP Journal on Advances in Signal Processing, vol. 2012, no. 86, Apr. 2012, pp.1-17.

[13] I.-O. Choi, S.-H. Park, M. Kim, K.-B. Kang, and K.-T. Kim, Efficient discrimination of ballistic targets with micromotions, IEEE Transactions on Aerospace and Electronic Systems, vol. 56, no. 2, Apr. 2020, pp.1243-1261.

[14] A. Persico, C. Clemente, D. Gaglione, C. Ilioudis, J. Cao, L. Pallotta, A. Maio, I. Proudler, and J. Soraghan, On model, algorithms, and experiment for micro-Doppler-based recognition of ballistic targets, IEEE Transactions on Aerospace and Electronic Systems, vol. 53, no. 3, Jun. 2017, pp.1088-1108.

[15] L. Rabiner, and B. Juang, An introduction to hidden Markov models, IEEE ASSP Magazine, vol. 3, no. 1, Jan 1986, pp.4-16.

[16] S. Ji, X. Liao, and L. Carin, Adaptive multiaspect target classification and detection with hidden Markov models, IEEE Sensors, vol. 5, no. 5, Oct. 2005, pp.1035-1042.

[17] D. Moody, and L. Joiner, Aspect angle estimation using fixed-rate hidden Markov models, in Conf. IEEE Radar, Ohio, 2014, pp.44-49.

[18] M. Athans, R. Whiting, and M. Gruber, A suboptimal estimation algorithm with probabilistic editing for false measurements with applications to target tracking with wake phenomena, IEEE Transactions on Automatic Control, vol. 22, no. 3, Jun. 1977, pp. 372-384.

[19] R. Mehra, A comparison of several nonlinear filters for re-entry vehicle tracking, IEEE Transactions on Automatic Control, vol. 16, no. 4, Aug. 1971, pp. 307-319.